Tilmann, F., Zhang, Y., Moreno, M., Saul, J., Eckelmann, F., Palo, M., Deng, Z., Babeyko, A. Y., Chen, K., Baez, J. C., Schurr, B., Wang, R., Dahm, T. (2016): The 2015 Illapel earthquake, central Chile: a type case for a characteristic earthquake? - *Geophysical Research Letters*, *43*, 2, pp. 574–583.

DOI: http://doi.org/10.1002/2015GL066963

AGU PUBLICATIONS

Geophysical Research Letters

RESEARCH LETTER
10.1002/2015GL066963

Key Points:
- We determine a comprehensive rupture model for the 2015 Illapel earthquake
- Divergence between finite fault and backprojection source time functions indicates shallow slip
- The 1943 Illapel earthquake rupture was probably similar in the deeper parts but lacks shallow slip

Supporting Information:
- Texts S1–S7, Figures S1–S15, and Tables S1 and S2

Correspondence to:
F. Tilmann,
tilmann@gfz-potsdam.de

Citation:
Tilmann, F., et al. (2016), The 2015 Illapel earthquake, central Chile: A type case for a characteristic earthquake?, *Geophys. Res. Lett.*, *43*, 574–583, doi:10.1002/2015GL066963.

Received 9 NOV 2015
Accepted 23 DEC 2015
Accepted article online 30 DEC 2015
Published online 19 JAN 2016

The 2015 Illapel earthquake, central Chile: A type case for a characteristic earthquake?

F. Tilmann[1,2], Y. Zhang[3], M. Moreno[1], J. Saul[1], F. Eckelmann[1], M. Palo[1], Z. Deng[1], A. Babeyko[1], K. Chen[1], J. C. Baez[4], B. Schurr[1], R. Wang[1], and T. Dahm[1,5]

[1]Deutsches GeoForschungsZentrum GFZ, Potsdam, Germany, [2]Freie Universität Berlin, Berlin, Germany, [3]School of Earth and Space Sciences, Peking University, Beijing, China, [4]Centro Sismológico Nacional, Universidad de Chile, Santiago de Chile, Chile, [5]Universität Potsdam, Potsdam, Germany

Abstract On 16 September 2015, the M_W = 8.2 Illapel megathrust earthquake ruptured the Central Chilean margin. Combining inversions of displacement measurements and seismic waveforms with high frequency (HF) teleseismic backprojection, we derive a comprehensive description of the rupture, which also predicts deep ocean tsunami wave heights. We further determine moment tensors and obtain accurate depth estimates for the aftershock sequence. The earthquake nucleated near the coast but then propagated to the north and updip, attaining a peak slip of 5–6 m. In contrast, HF seismic radiation is mostly emitted downdip of the region of intense slip and arrests earlier than the long period rupture, indicating smooth slip along the shallow plate interface in the final phase. A superficially similar earthquake in 1943 with a similar aftershock zone had a much shorter source time function, which matches the duration of HF seismic radiation in the recent event, indicating that the 1943 event lacked the shallow slip.

1. Introduction

The idea that segmentation of plate boundary faults controls nucleation points and rupture sizes of large and great earthquakes [e.g., *Ando*, 1975] has been around for a long time, but due to the limited earthquake history is not straightforward to confirm, particularly in subduction zones. Whereas step overs and other fault complexity make segmentation relatively easy to map in strike-slip faults [*Wesnousky*, 2006; *Toksöz et al.*, 1979], this task is more difficult in subduction zones, where the subduction megathrust is buried and its geometry can thus not be constrained to the same level of detail. The Chilean margin is well suited to study margin segmentation because of its well known earthquake history, because of its relatively simple geometry avoiding large changes to the obliquity and rate of plate subduction, and because of the high rate of convergence, which results in a quick build up of stress and in turn the generation of many great earthquakes during the instrumental era. In addition, a dense network of Global Navigation Satellite Systems (GNSS) stations has been built up over the last decade, allowing—in combination with the availability of large-scale seismological arrays (USArray, European Broadband network, and HINET array)—detailed modeling of the rupture of recent large earthquakes.

On 16 September 2015, the Chilean margin produced another great earthquake which nucleated near the coast of the Coquimbo province in central Chile and grew into a rupture with moment magnitude (M_W) of 8.2 (GCMT and GEOFON) to 8.3 (U.S. Geological Survey, USGS). The earthquake caused a sizeable tsunami with peak height of 4.5 m measured at the Coquimbo tide gauge and ~2 m in Valparaíso (from http://www.ioc-sealevelmonitoring.org/station.php?code=coqu). Damage from the tsunami was extensive, with a strip hundreds of meters inland from the shoreline devastated in the most strongly affected areas, but thanks to the exemplary emergency response involving the evacuation of more than one million people only, 16 fatalities were reported.

In this study we draw on a variety of geodetic and seismological data sets in order to constrain the coseismic rupture process in detail. Further, we locate and determine moment tensors for larger aftershocks based on regional and teleseismic data and compare both slip distribution and aftershock sequence to previous earthquakes.

2. Tectonic Setting

The area has last been hit by a great earthquake in 1943, estimated to be slightly smaller at M_W = 7.8–7.9 by *Beck et al.* [1998] (Figure 1). The area immediately to the north ruptured in 1922 in a much larger earthquake,

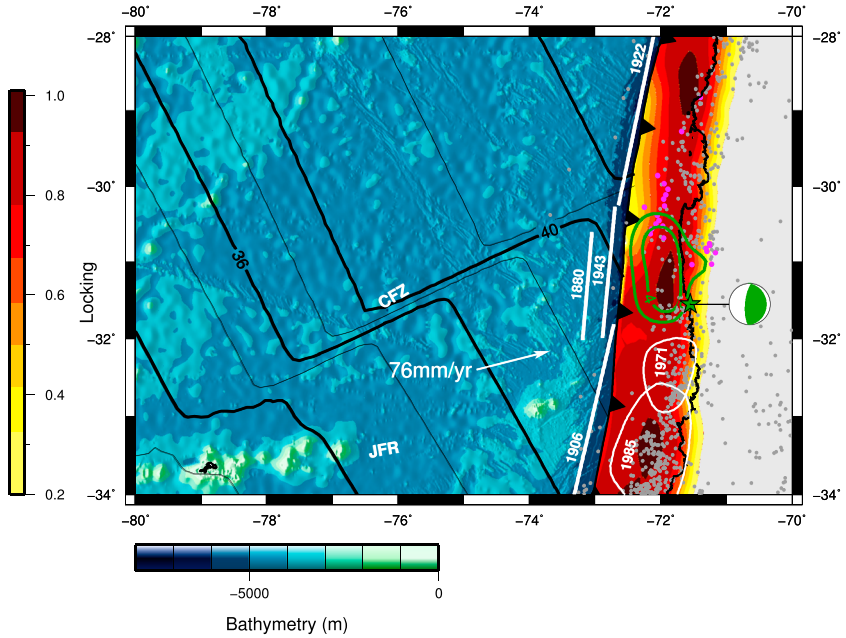

Figure 1. Map of the study area with incoming seafloor relief [*Smith and Sandwell*, 1997] shown seaward of the deformation front and the locking model (Text S3.4 in the supporting information) landward of it. Black contours show 2 Ma increments of oceanic plate age [*Müller et al.*, 2008]. Two-meter coseismic slip contours are shown in dark green (this study). White lines indicates aftershock area of 1971 and 1985 according to *Comte et al.* [1986], and white bars mark the approximate along-strike extent of historical ruptures (after compilation in *Beck et al.* [1998] and *Kelleher* [1972]). Earthquakes with magnitude greater or equal 5.0 between 1963 and just before the Illapel event are shown as gray dots (Engdahl catalog up to 2008 [*Engdahl et al.*, 1998] and ISC bulletin from 2009 onward) with events between July 1997 and January 1998 plotted in magenta in order to highlight the events of the Coquimbo swarm. The main shock epicenter and focal mechanism are also marked (both GEOFON catalog). Plate convergence is shown for MORVEL plate model [*DeMets et al.*, 2010]. JFR is the Juan-Fernandez Ridge, and CFZ is the Challenger Fracture Zone.

whereas to the south earthquakes in 1971 and 1985 broke the coupled interface and partially overlap with the 2010 Maule earthquake. A patch of relatively low interseismic coupling was inferred between the rupture areas of the 1922 and 1943 events at ~30°S by *Métois et al.* [2012] and is also seen in our coupling model (Figure 1) (see Text S3.4 in the supporting information). The area between this boundary and the northern edge of the 2010 Maule earthquake is termed the Metropolitan segment [e.g., *Métois et al.*, 2012]. In 1997 the region 29.6°–31°S experienced swarm-like activity (Coquimbo swarm), which included several $M_W > 6$ events and involved both the plate interface and intraplate events within the downgoing plate [*Lemoine et al.*, 2001] (Figure 1).

The major bathymetric feature in the area is the Juan-Fernandez Ridge (JFR), a hot spot chain, which intersects the trench near 32.5°S. The ridge blocks northward flow of sediments, yielding a sharp contrast between a trench filled with ample sediment in the south to a sediment starved trench with less than 1 km of sediments within the Metropolitan segment [*Contreras-Reyes et al.*, 2015]. As a direct result of the contrasting sediment thickness, the subduction style changes from accretionary in the south to erosive in the north [*von Huene et al.*, 1997]. The JFR further marks the transition to flat slab subduction in the north [*Pardo et al.*, 2002], but the slab interface at seismogenic depths ($\lesssim$50 km depth) has a dip of 20–22°both to to the north and south (*Lange et al.* [2012], *Hayes et al.* [2012], and this study). In the north the Challenger Fracture Zone (CFZ), which intersects the margin at 30°S, is associated with an age offset of 3.5 Myr but does not exhibit significant relief (Figure 1).

3. Coseismic Rupture

Displacements measured at continuous GNSS stations (Figure S4) indicate uplift of the coastline and westward motion approximately radially toward a point offshore near 31.2°S. Nearfield interferometric synthetic

aperture radar (InSAR) fringes also align along a circular pattern (Figure S1) focused on this area. These observations point to a simple rupture with peak slip located offshore at this latitude.

We applied different approaches for inferring coseismic slip and rupture evolution. First, we model the coseismic displacement field as recorded by continuous GNSS stations using a realistic geometry for the plate interface (SLAB1.0) [*Hayes et al.*, 2012] and laterally heterogeneous elastic structure [*Tassara and Echaurren*, 2012], following the methodology of *Moreno et al.* [2012] (see Text S3 for more detail). In Figures 1 and 3 we show the model for the purely coseismic displacement, but using the same geometry, we also calculated the model based on the daily GNSS solution and InSAR data, which also includes the effects of the first day of postseismic slip including an $M_W = 7.0$ aftershock, shown in Figures S4 and S11b. In a second approach, we model the waveforms at 22 azimuthally well-distributed stations at teleseismic distances in order to invert for slip along a planar rupture interface defined by the shallow dipping fault plane of the moment tensor solution (see Text S4). This inversion is also constrained by strong motion and high-rate GPS waveforms, and static displacements from GNSS stations and InSAR. A third view of the rupture is provided by the backpropagation of seismic arrivals at North American stations. The data are filtered between 1 and 4 Hz, and the potential emission point corresponding to the highest semblance at each time step is identified as an emitter of high-frequency seismic radiation (HFSR) (see Text S5). HFSR tracks the progression of the rupture but is not proportional to slip. Instead, HFSR is emitted where there are strong changes to the slip or rupture propagation velocity. For a perfectly smooth rupture, HFSR would only be emitted at the onset and arrest of the rupture, but in realistic ruptures HFSR tracks rough parts of the rupture process.

The coseismic slip estimated by the former two methods results in a broadly similar rupture pattern (Figures 2 and S11), albeit with a somewhat different peak slip of ~6 m and 4.8 m in the geodetic finite element model and joint inversion models, respectively. The geodetic solution also has a more elongated region of maximum slip. In agreement with the relatively simple slip pattern, the moment rate function is shaped like a triangle, except for a separate low-energy nucleation phase of 15 s duration, during which the rupture stays close to the nucleation point. The nucleation phase is seen both in the kinematic model, where the rupture expands, but stays centered on the hypocenter and in the backprojection results, where small amounts of HFSR are emitted from points very close to the hypocenter. This phase is associated with only moderate cumulative slip of less than 2 m. In the latter phase the rupture propagates northward and updip, gaining in strength in the process. The HFSR tracks the northward propagation, marking approximately the deeper edge of significant coseismic slip. In the final phase of the rupture, finite slip has moved to the near-trench region and no significant HFSR can be detected anymore. This may indicate a long rise time and ongoing smooth slip.

The concentration of HFSR at the downdip edge of coseismic slip has been observed for most recent great megathrust earthquakes (e.g., Tohoku) [*Koper et al.*, 2011, Maule *Kiser and Ishii*, 2012; *Palo et al.*, 2014] but not all: for the Iquique earthquake coseismic slip evolution and HFSR seem to be related more closely although the HFSR still occurs slightly downdip of the peak slip [*Schurr et al.*, 2014]. The absence of HFSR during the final phase of the rupture is maybe also unsurprising as then little to no slip occurs in the region which is capable of generating HFSR, with the shallow interface generally seen as an area where slip tends to progress slowly when it does propagate into this region at all [*Bilek et al.*, 2004].

Although we did not invert DART buoy observations, we calculated predicted tsunami wave heights at three buoys (see Text S6). We note that the horizontal motion of the seafloor in the area of the steep forearc topography makes a significant contribution to the tsunami amplitudes for this earthquake. In spite of the differences in peak slip both the geodetic and joint inversion model can fit amplitude and approximate timing of the leading wave of the tsunami (Figures 2d and S15). As all the buoys are in a low-energy lobe of the tsunami radiation pattern, directivity effects result in a strong dependence on the strike of the rupture. Here we find that the joint inversion result assuming the strike of the GEOFON moment tensor solution somewhat underpredicts the tsunami amplitudes.

4. Aftershock Distribution

As expected for an earthquake of this size, the aftershock activity in the following weeks was high. Our catalog of aftershocks for the first five weeks comprises 215 events above M_W 4. Clear depth phases (pP and sP) observed at teleseismic distances allowed us to constrain focal depth to within a few kilometers for most events (see Text S7). This is particularly important for offshore events for which onshore local network locations tend to be less reliable. We augment the catalog of aftershocks by identifying peaks in the semblance

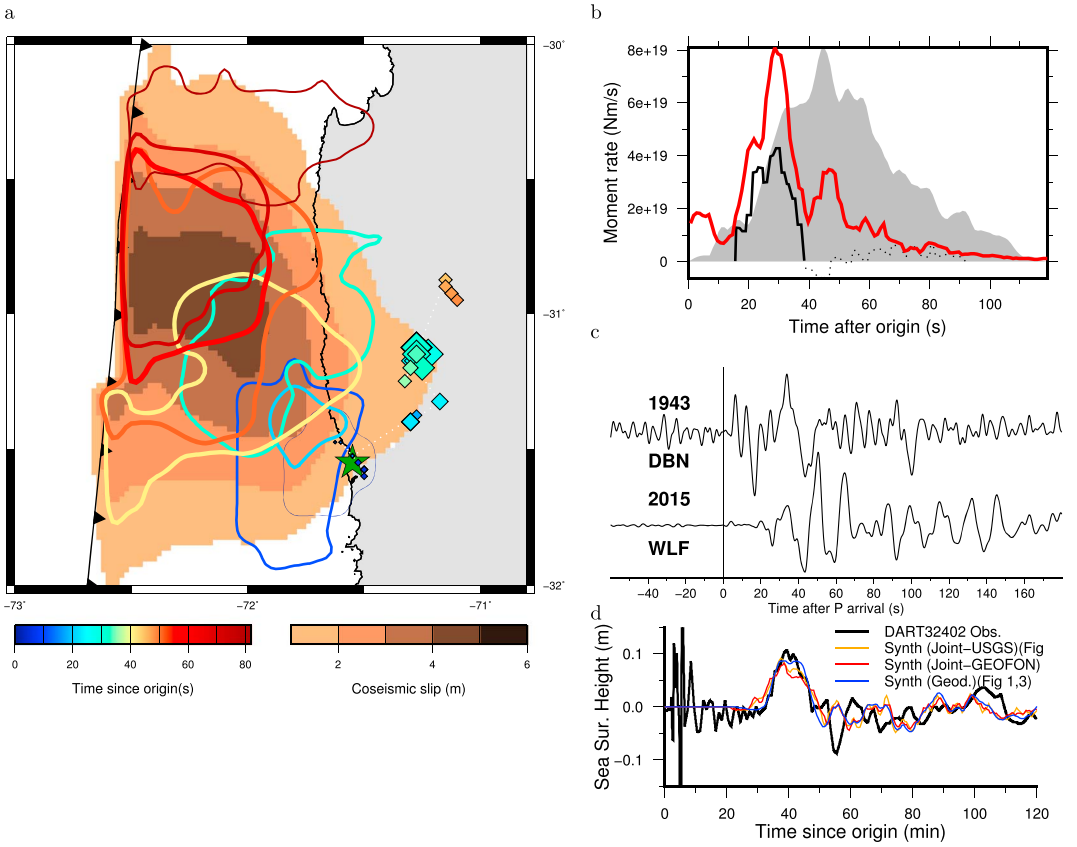

Figure 2. Coseismic slip model. (a) The color image shows the dip component of coseismic slip in the joint inversion model, with slip less than 1 m omitted, as this is not well constrained. The slip evolution in the finite frequency model is visualized for frames every 10 s; the contours are drawn at 50% of the instantaneous slip rate maximum, with their color indicating time since origin and their thickness being scaled according to the maximum slip rate in the frame. Diamonds show emission of HFSR (1–4 Hz) throughout the rupture (plotted every second); their size is scaled according to the peak energy of the stack, and only points with associated semblance of more than 0.06 are plotted. (b) Comparison of the moment rate function estimated from finite fault inversion (gray) and history of peak backprojected energy in each time frame (red line), and moment rate function for the 1943 event from *Beck et al.* [1998] (black line), shifted by 12 s to latter times for visualization purposes and in order to line up the main phases of both events; a weak nucleation phase like that in the 2015 earthquake might have been missed in the historical data or been absent. The units of backprojected energy are arbitrary. The secondary peak of the backprojected energy at ~45 s, corresponding to the northeasternmost emission points (orange diamonds) is probably real but could also be the depth phase echo (more likely sP than pP) of the main peak at ~30 s. The 1943 moment rate function becomes negative after the initial peak, and its later evolution (shown by dashed line) is likely to reflect propagation rather than source effects. (c) *P* wave seismogram comparison between 1943 earthquake, recorded in DeBilt with a Galitzin seismograph (epicentral distance $\Delta = 107°$), and 2015 earthquake, recorded at Walferdange, Luxembourg ($\Delta = 106°$), recorded with a modern broadband instrument but shown with a simulated Galitzin response. (d) Comparison of observed and modeled tsunami waveforms at DART buoy 32402. See Figure S14 for location of buoy and Figure S15 for other stations.

of backprojected waveforms in the first 6 h of waveform data after the main shock. In addition, we computed 109 moment tensors for most events above approximately M_W 4.5. The dominant type of aftershocks are shallowly dipping thrust events with a dip consistent with slip on the plate interface (Figures 3 and 4). Although depths scatter by 5–10 km, this scatter can be attributed to uncertainty of the depth determination and does not contradict a plate interface origin for the shallowly dipping thrust events.

The largest aftershocks (up to *M*7.0) occurred in the epicentral area, and this area remains the focus of the most intense aftershock activity throughout at least the first month of the aftershock sequence, alongside another area near the coast at the northern rupture limit (~31.5°S). The small amount of slip in these areas agrees with the idea that aftershocks—or aseismic creep loading the patches on which aftershocks occur—fill slip deficits left behind by the main rupture [e.g., *Perfettini et al.*, 2010; *Kiser and Ishii*, 2013], but raises the question, "why has slip progressed so reluctantly in the first phase of the rupture?" In fact, the nucleation area might

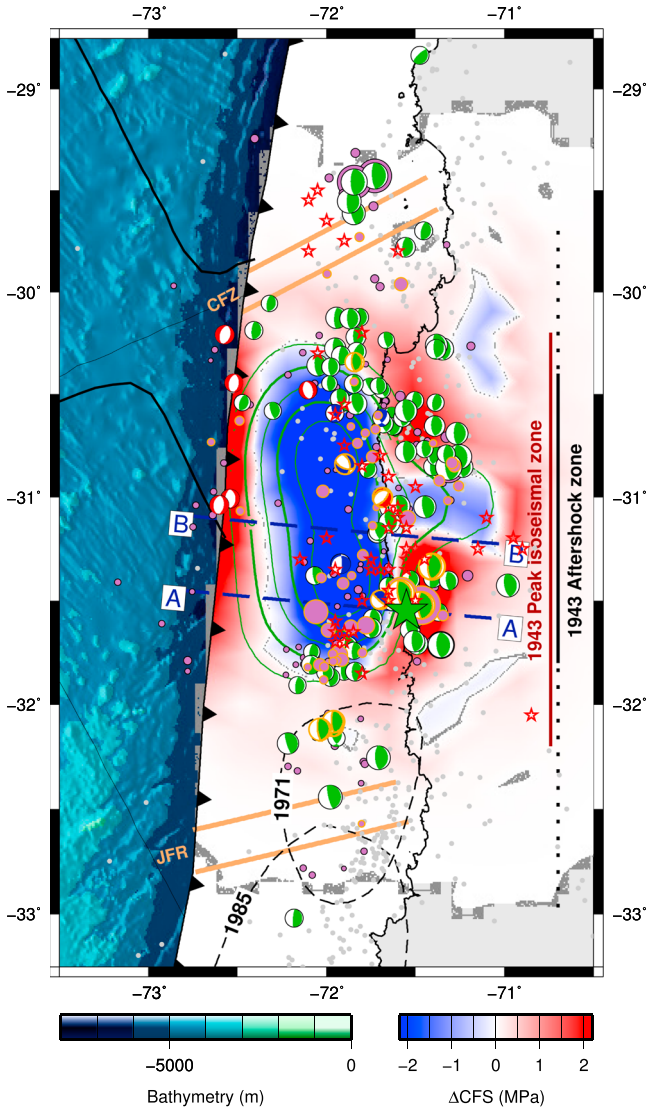

Figure 3. Distribution of aftershocks until 15 December 2015 (with $M > 4$, estimated magnitude of completeness $M = 4.5$). Orange outline marks events which have occurred within 24 h of the main shock, including an M_W7.0 event just 24 min after the main shock and close to its epicenter, the largest aftershock so far. Small stars mark additional events during the first hour identified by backprojection analysis (only epicenter available). Events with focal mechanism are color coded by mechanism type: green thrusts, red normal faulting, and blue oblique. Dotted blue lines show locations of cross sections shown in Figure 4. The 1943 aftershock and isoseismal zone is after *Kelleher* [1972]. Orange lines show extrapolated traces of subducted JFR and CFZ. The background image shows the coseismic change in Coulomb Failure Stress (CFS). Other elements as in Figure 1.

have been less strongly coupled to begin with; nucleation and later aftershock activity on less coupled parts of the megathrust have been clearly observed in other great megathrust earthquakes, e.g., Maule 2010, [*Lorito et al.*, 2011] and Nias 2005 [*Chlieh et al.*, 2008; *Tilmann et al.*, 2010], and this interpretation is consistent with the locking model (Figure 1). Plate interface seismicity extends along-strike well beyond the coseismic rupture by approximately 75 km in the south to 50 km in the north (Figure 3). Events in these areas occurred very soon after the rupture: the distribution of events during the first 24 h (red circles events in Figure 3) does not deviate significantly from their distribution over the first week. This fairly rapid triggering points to static Coulomb failure stress changes (ΔCFS) induced by the main shock as the primary triggering mechanisms rather than aseismic creep. The predicted ΔCFS at the furthest points at which unarguably aftershocks occur is 0.2 MPa in the south (at 32.3°S 72°W) and 0.018 MPa in the north (at 29.5°S, 71.9°W) (Figure 3, calculated for the geodetic model). The exact values are quite sensitive to the details of the rupture model, but it is clear they are above

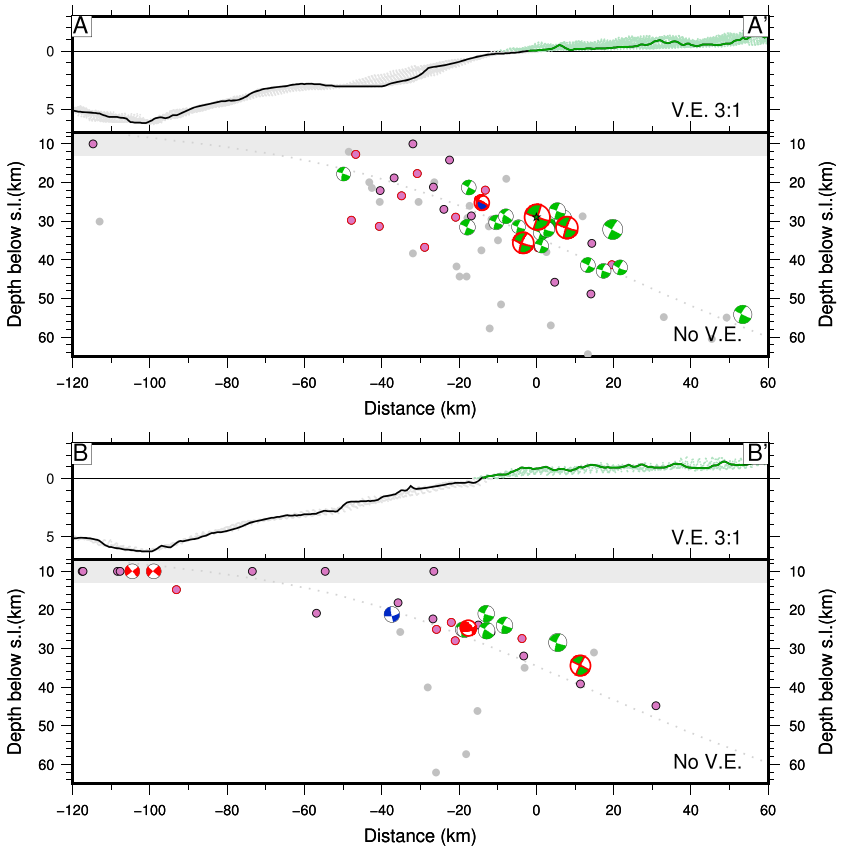

Figure 4. Cross sections. Focal mechanisms are plotted in the hemisphere-behind-vertical plane convention, and the dotted line marks the top of the slab in the SLAB1.0 model [*Hayes et al.*, 2012]. The swath width is 20 km in both directions. Cross-section A passes through the hypocenter and the surrounding cluster of strong aftershock activity. Cross-section B shows activity in the outer rise area. Tops of plots show topography along the profile (dots along the profile show variability within the swath). For very shallow events, it is not possible to constrain the depth using regional and teleseismic data, and the depth is therefore fixed at a nominal depth of 10 km; this depth range is marked with a gray background in the figure.

the ΔCFS values where triggered activity has been demonstrated in previous studies [*Seeber and Armbruster*, 2000; *Ziv and Rubin*, 2000]. Qualitatively, we see a good agreement between aftershock locations and areas of enhanced CFS, most notably the two patches downdip of the rupture just mentioned (Figure 3). The strong increase in CFS predicted for the shallow plate interface is not associated with corresponding seismic activities, but here, generally, frictional properties are such that earthquakes cannot nucleate, even if some slip can occur as part of larger rupture. However, the group of earthquakes within the lobe of negative ΔCFS extending to the east of the coastline is unexpected in this context.

The second most important group of aftershocks comprises normal faulting events in the oceanic plate. Most of these are located close to the trench and can be considered outer rise events resulting from a combination of bending and horizontal tensional stresses. These types of events often follow great subduction earthquakes as a result of increased tensional load [e.g., *Lay et al.*, 1989], particularly where the shallow part of the plate interface has ruptured and adjacent to the main slip patches, a pattern observable both in the Maule [*Lange et al.*, 2012; *Agurto et al.*, 2012; *Hayes et al.*, 2013] and Tohoku aftershock sequences [*Sato et al.*, 2012]. In contrast, hardly any normal-faulting events were observed following the 2014 Iquique earthquake and none near the trench in spite of the similar moment magnitudes of the Iquique and Illapel earthquakes. This difference in outer rise response confirms that the Illapel earthquake ruptured onto a shallower part of the plate interface than the Iquique earthquake, including possible slip right to the trench. A few normal-faulting events occured below the forearc and close to the expected interface, making it difficult to decide whether they have ruptured in the continental or oceanic plate. In any case, shallow normal faulting aftershocks in the forearc, which were so prominent in the Maule and Tohoku aftershock sequences [*Ryder et al.*, 2012; *Farías et al.*, 2011;

Ruiz et al., 2014; *Kato et al.*, 2011], are notably absent in spite of the presence of a prominent, apparently active normal fault in a seismic reflection profile at 31°S ~25 km offshore [*Contreras-Reyes et al.*, 2015].

Also in contrast to the Iquique and Maule earthquakes, there is only very little aftershock activity in the forearc crust; the only events of this type with moment tensors are oblique thrusts occurring in the parts of the segment having experienced little slip during the main event.

5. Discussion and Conclusion

Taking into account the coseismic slip modeling results, the tsunami buoy pressure records, and the backprojection results, it appears that the Illapel earthquake has ruptured across the width of the seismogenic zone. Rupture thus initiated at the downdip end of the primary seismogenic zone (domain B in terminology of *Lay et al.* [2012], which will be used throughout the discussion) and took in both the shallow part of the megathrust, particularly important for tsunami excitation (domain A) and the deeper part (domain C), which most efficiently generates HFSR and is responsible for most of the shaking; reported intensities were VIII-IX adjacent to the rupture zone in the DYFI database of the USGS (http://earthquake.usgs.gov/earthquakes/eventpage/us20003k7a#impact_dyfi, accessed 26 October 2015), and the highest instrumentally recorded peak ground acceleration was 0.75 g.

The along-strike extent of the Illapel rupture coincides approximately with a local high in interseismic locking in our updated locking map (Figure 1). A similar pattern is found in the locking map of *Métois et al.* [2012]. The updip extent of locking is very hard to constrain such that the shift in dip direction between peak slip and maximum locking is not significant. The aftershocks extend into the areas of intermediate locking to the south and north. *Métois et al.* [2012] had already pointed out the possible role of incoming seafloor features, i.e., the JFR and CFZ, in controlling the segment boundaries as their projection below the forearc approximately coincides with the region of low locking. However, the actual coseismic rupture is clearly much smaller than the gap between these features (Figure 1), such that it is hard to make the argument that the main shock rupture was arrested by either of them. In fact, fracture zones are unlikely candidates for arresting ruptures because the 1960 Chile earthquake ruptured through the southern Chile margin across the entry points of several prominent fracture zones with age offsets exceeding that of the CFZ and more bathymetric relief. Instead, the projections of the JFR and CFZ below the margin seem to mark the limits of significant aftershock activity (the larger event near 33°S could easily be a coincidental independent event). The coincidence of the entry point of a seamount chain with the limits of the aftershock zone, rather than with the main shock rupture zone limits, was also observed for the Tohoku earthquake [*Shinohara et al.*, 2012].

The presence of a local high in locking and the fact that prior earthquakes in 1943 and 1880 seem to have broken a similar part of the margin justify the identification of the area between 30°and 32°S as a distinct segment [*Métois et al.*, 2012, 2014], even though in the earlier earthquake history its southern boundary seems to have been breached by earthquakes in 1730 and maybe in 1647 [*Beck et al.*, 1998]. The accumulated margin-normal slip deficit since 1943 is 5.31 m for full locking (based on convergence of 78 mm/year at 19°obliqueness) [*DeMets et al.*, 2010], similar to the actual peak slip of the Illapel earthquake. Leaving the case of the eighteenth century multisegment rupture aside, the Coquimbo-Illapel margin thus seems to be an ideal host for characteristic earthquakes, i.e., earthquakes with very similar properties in subsequent seismic cycles. The rupture extent of the 1943 earthquake as estimated from isoseismal contours, appears to be broadly similar to that of the recent earthquake but extends further south (Figure 3). Peak intensities of IX-X on the Mercalli-Sieberg scale are also comparable (*Beck et al.* [1998] citing *Kelleher* [1972] and unpublished map by F. Greve [1946]). Only a few aftershocks were located teleseismically such that their along-strike extent (30.4° – 31.8°S) is maybe not representative. Instead, *Kelleher* [1972] used S-P times recorded at LaPaz, Bolivia, to estimate the extent of the aftershock zone (29.7° – 33°S), which is remarkably similar to the present aftershock sequence (Figure 3), although unfortunately it is not clear from Kelleher's paper how well constrained that range is.

In contrast to this superficial similarity stands the much smaller seismic moment determined for the 1943 event by *Beck et al.*, 1998 (6×10^{20} Nm, only about a fourth of the moment of the recent event). Whereas the amplification of some of the historical records used may be poorly determined [*Beck et al.*, 1998], *Beck et al.*, 1998 also infer a much briefer source time function of only ~25 s duration, with peak slip attained after 17 s (Figure 2b). Even if we discount the early weak phase of the 2015 shock it is clear that the recent event ruptured at least twice as long. In fact, the very different source characteristics are immediately obvious from

a direct comparison of the recordings of the 2015 and 1943 earthquakes at similar distances, which show a much longer long-period *P* wave phase for the 2015 event (Figure 2c). The difference in moment cannot be explained by the difference in recurrence time (63 years between 1880 and 1943, and 82 years between 1943 and 2015), most clearly so when the slip in the 1943 event is estimated by assuming identical rupture areas (as indicated by the similar aftershock areas, implying the slip in 1943 would have been about one fourth of the slip in 2015, i.e., 1–1.5 m), less clearly but still visibly so from scaling relations (which predict the 2015 event to have 2.5 times the area of the 1943 event; i.e., relative to the four times larger moment, an average slip 1.6 times smaller than the slip observed now would be inferred). Indeed, based on the similar along-strike extent and intensities one may speculate that the 1943 event lacked the final rupture phase where slip occurred predominantly in the shallowest part of the interface. Incidentally, the 1943 moment rate function has a similar length as the HFSR time evolution (Figure 2b). In contrast, a similar time evolution of HFSR time history and moment rate function was observed for the Iquique earthquake [*Schurr et al.*, 2014], which did not rupture the shallow interface. Therefore, the rupture on the deeper part of the subduction interface (in domains B and C) was potentially quite similar for the 1943 and 2015 events, albeit somewhat smaller slip would have been required for the 1943 event based on its lower estimated moment. If the shallow megathrust is only partially coupled, it might require several seismic cycles of the central part of the interface (domain B) to accumulate sufficient slip deficit for failure to occur there (domain A). Of course, this also implies that shallow postseismic slip, if it occurred at all following the 1943 event, should not fully compensate the slip deficit. The possible longer interval between ruptures on the shallowest part of the plate interface might be the reason why globally tsunami earthquakes, i.e., earthquakes which have almost all their slip concentrated in the shallow part of the interface and which generate tsunamis disproportionately large relative to their seismic moment [*Kanamori*, 1972], are rare. Alternatively, one can hypothesize that the 1943 earthquake released the accumulated shear stress only incompletely. In a time-predictable earthquake scenario this would imply that the 1880 event also caused similarly sized, equally incomplete stress release. However, as locking is complete, the peak slip in 2015 would have been expected to exceed the slip deficit accumulated since 1943, contrary to observations. In either scenario, it is curious that the 1997 Coquimbo swarm did not trigger a major interface event earlier, as the suggestion put forward by *Lay et al.* [2014] that this segment is accumulating interseismic stress more slowly is all but disproven by the recent event. It seems that we might simply have to accept the highly complex nature of the earthquake generation process, where the strong dependence on initial conditions—such as the prestress left behind by historical earthquakes—makes it almost impossible to predict the size of future ruptures with any confidence, even if the interseismic stress accumulation (locking model) is constant and known [*Nic Bhloscaidh et al.*, 2015].

In conclusion even this simple segment does not seem to produce characteristic earthquakes in the strict sense, and slip predictability can be rejected. This finding is consistent with statistical approaches, which find that the frequency-magnitude distributions determined for the major subduction zones are consistent with the standard Gutenberg-Richter power law distribution, contrary to the prediction of the characteristic earthquake hypothesis [*Naylor et al.*, 2009]. Considering the events in 1971, 1985, and 2010, the area to the south has arguably completed its seismic cycle for this generation, and no $M > 8$ earthquake is expected there in the near future. This throws the spotlight on the Atacama segment to the north, which has ruptured in a great earthquake in 1922 and has not experienced an event with $M > 7.5$ since but is likely to be further loaded by the postseismic response to the Illapel earthquake in the months to come. This segment thus remains at significant risk for another great earthquake and accompanying tsunami.

Acknowledgments
We acknowledge the French-Chilean International Associated Laboratory (LIA) and CSN geodetic networks for giving access to data of several of their continuous cGPS stations in Chile. Seismological data from the FDSN networks C, C1, CX, BL, GE, GT, II, IU, and G were used for aftershock location and moment tensor determination and IU for the main shock rupture model. Thanks to Bernhard Dost (KNMI) for providing the scan of the 1943 seismogram, and Galina Kulikova for digitizing it. John McCloskey and an anonymous reviewer provided very helpful and supportive reviews.

References

Agurto, H., A. Rietbrock, I. Ryder, and M. Miller (2012), Seismic-afterslip characterization of the 2010 M_W 8.8 Maule, Chile, earthquake based on moment tensor inversion, *Geophys. Res. Let.*, *39*, L20303, doi:10.1029/2012GL053434.

Ando, M. (1975), Source mechanisms and tectonic significance of historical earthquakes along the Nankai Trough, Japan, *Tectonophysics*, *27*, 119–140.

Beck, S., S. Barrientos, E. Kausel, and M. Reyes (1998), Source characteristics of historic earthquakes along the central Chile subduction zone, *J. South Am. Earth Sci.*, *11*, 115–129.

Bilek, S. L., T. Lay, and L. J. Ruff (2004), Radiated seismic energy and earthquake source duration variations from teleseismic source time functions for shallow subduction zone thrust earthquakes, *J. Geophys. Res.*, *109*, B09308, doi:10.1029/2004JB003039.

Chlieh, M., J. P. Avouac, K. Sieh, D. H. Natawidjaja, and J. Galetzka (2008), Heterogeneous coupling of the Sumatran megathrust constrained by geodetic and paleogeodetic measurements, *J. Geophys. Res.*, *113*, B05305, doi:10.1029/2007JB004981.

Comte, D., A. Eisenberg, E. Lorca, M. Pardo, L. Ponce, R. Saragoni, S. Singh, and G. Suarez (1986), The 1985 Central Chile earthquake: A repeat of previous great earthquakes in the region?, *Science*, *233*, 449–452.

Contreras-Reyes, E., J. A. Ruiz, J. Becerra, H. Kopp, C. Reichert, A. Maksymowicz, and C. Arriagada (2015), Structure and tectonics of the central Chilean margin (31°–33°S): Implications for subduction erosion and shallow crustal seismicity, *Geophys. J. Int.*, *203*, 776–791, doi:10.1093/gji/ggv309.

DeMets, C., R. G. Gordon, and D. F. Argus (2010), Geologically current plate motions, *Geophys. J. Int.*, *181*(1), 1–80, doi:10.1111/j.1365-246x.2009.04491.x.

Engdahl, E., R. D. van der Hilst, and R. P. Buland (1998), Global teleseismic earthquake relocation with improved travel times and procedures for depth determination, *Bul. Seismol. Soc. Am.*, *88*, 722–743.

Farías, M., D. Comte, S. Roecker, D. Carrizo, and M. Pardo (2011), Crustal extensional faulting triggered by the 2010 Chilean earthquake: The Pichelemu seismic sequence, *Tectonics*, *30*, TC6010, doi:10.1029/2011TC002888.

Hayes, G. P., D. J. Wald, and R. L. Johnson (2012), Slab1.0: A three-dimensional model of global subduction zone geometries, *J. Geophys. Res.*, *117*, B01302, doi:10.1029/2011JB008524.

Hayes, G. P., E. Bergman, K. L. Johnson, H. M. Benz, L. Brown, and A. S. Meltzer (2013), Seismotectonic framework of the 2010 February 27 M_W 8.8 Maule, Chile earthquake sequence, *Geophys. J. Int.*, *195*, 1034–1051, doi:10.1093/gji/ggt238.

Kanamori, H. (1972), Mechanism of tsunami earthquakes, *Phys. Earth Planet. Int.*, *6*, 346–359.

Kato, A., S. Sakai, and K. Obara (2011), A normal-faulting seismic sequence triggered by the 2011 off the Pacific coast of Tohoku Earthquake: Wholesale stress regime changes in the upper plate, *Earth Planets Space*, *63*(7), 745–748, doi:10.5047/eps.2011.06.014.

Kelleher, J. (1972), Rupture zones of large South American earthquakes and some predictions, *J. Geophys. Res.*, *77*, 2089–2103.

Kiser, E., and M. Ishii (2012), Combining seismic arrays to image the high-frequency characteristics of large earthquakes, *Geophys. J. Int.*, *188*, 1117–1128, doi:10.1111/j.1365-246X.2011.05299.x.

Kiser, E., and M. Ishii (2013), The 2010 Maule, Chile, coseismic gap and its relationship to the 25 March 2012 Mw 7.1 Earthquake, *Bull. Seismol. Soc. Am.*, *103*, 1148–1153, doi:10.1785/0120120209.

Koper, K. D., A. R. Hutko, T. Lay, C. J. Ammon, and H. Kanamori (2011), Frequency-dependent rupture process of the 2011 M_W 9.0 Tohoku Earthquake: Comparison of short-period P wave backprojection images and broadband seismic rupture models, *Earth Planets Space*, *63*(7), 599–602, doi:10.5047/eps.2011.05.026.

Lange, D., F. Tilmann, S. E. Barrientos, E. Contreras-Reyes, P. Methe, M. Moreno, B. Heit, H. Agurto, P. Bernard, J.-P. Vilotte, and S. Beck (2012), Aftershock seismicity of the 27 February 2010 M_W 8.8 Maule earthquake rupture zone, *Earth Planet. Sci. Let.*, *317-318*, 413–425, doi:10.1016/j.epsl.2011.11.034.

Lay, T., L. Astiz, H. Kanamori, and D. H. Christensen (1989), Temporal variation of large intraplate earthquakes in coupled subduction zones, *Phys. Earth Planet. Int.*, *54*, 258–312.

Lay, T., H. Kanamori, C. Ammon, K. D. Koper, A. R. Hutko, Y. Lingling, H. Yue, and M. Rushing (2012), Depth-varying properties of subduction zone megathrust faults, *J. Geophys. Res.*, *117*, B04311, doi:10.1029/2011JB009133.

Lay, T., Y. Han, E. Brodsky, and A. Chao (2014), The April 1, 2014 Iquique, Chile, M_W 8.1 earthquake rupture sequence, *Geophys. Res. Let.*, *41*, 3818–3825, doi:10.1002/2014GL060238.

Lemoine, A., R. Madariaga, and J. Campos (2001), Evidence for earthquake interaction in central Chile: The July 1997–September 1998 sequence, *Geophys. Res. Lett.*, *28*(14), 2743–2746, doi:10.1029/2000GL012314.

Lorito, S., F. Rommano, S. Atzori, X. Tong, A. Avallone, J. McCloskey, M. Cocco, E. Boschi, and A. Piatanesi (2011), Limited overlap between the seismic gap and coseismic slip of the great 2010 Chile earthquake, *Nat. Geosci.*, *4*, 173–177, doi:10.1038/ngeo1073.

Métois, M., A. Socquet, and C. Vigny (2012), Interseismic coupling, segmentation and mechanical behavior of the central Chile subduction zone, *J. Geophys. Res.*, *117*, B03406, doi:10.1029/2011JB008736.

Métois, M., C. Vigny, S. Socquet, A. Delorme, S. Morvan, I. Ortega, and C.-M Valderas-Bermejo (2014), GPS-derived interseismic coupling on the subduction and seismic hazards in the Atacama region, Chile, *Geophys. J. Int.*, *196*, 644–655, doi:10.1093/gji/ggt418.

Moreno, M., et al. (2012), Toward understanding tectonic control on the M_W 8.8 2010 Maule Chile earthquake, *Earth Planet. Sci. Let.*, *321-322*, 152–165, doi:10.1016/j.epsl.2012.01.006.

Müller, R. D., M. Sdrolias, C. Gaina, and W. Roest (2008), Age, spreading rates, and spreading asymmetry of the world's ocean crust, *Geochem. Geophys. Geosyst.*, *9*, Q0406, doi:10.1029/2007GC001743.

Naylor, M., J. Greenhough, J. McCloskey, A. F. Bell, and I. G. Main (2009), Statistical evaluation of characteristic earthquakes in the frequency-magnitude distributions of Sumatra and other subduction zone regions, *Geophys. Res. Lett.*, *36*, L20303, doi:10.1029/2009GL040460.

Nic Bhloscaidh, M., J. McCloskey, M. Naylor, S. Murphy, and A. Lindsay (2015), Reconstruction of the slip distribution in historical earthquakes on the Sunda megathrust, *W. Sumatra, Geophys. J. Int.*, *202*, 1339–1361, doi:10.1093/gji/ggv195.

Palo, M., F. Tilmann, F. Krüger, L. Ehlert, and D. Lange (2014), High-frequency seismic radiation from Maule earthquake (M_W 8.8, 2010 February 27) inferred from high-resolution backprojection analysis, *Geophys. J. Int.*, *199*, 1058–1077, doi:10.1093/gji/ggu311.

Pardo, M., D. Comte, and T. Monfret (2002), Seismotectonic and stress distribution in the central Chile subduction zone, *J. South Am. Earth Sci.*, *15*(1), 11–22, doi:10.1016/s0895-9811(02)00003-2.

Perfettini, H., et al. (2010), Seismic and aseismic slip on the Central Peru megathrust, *Nature*, *465*, 78–81, doi:10.1038/nature09062.

Ruiz, J. A., G. P. Hayes, D. Carrizo, H. Kanamori, A. Socquet, and D. Comte (2014), Seismological analyses of the 2010 March 11, Pichilemu, Chile Mw 7.0 and Mw 6.9 coastal intraplate earthquakes, *Geophys. J. Int.*, *197*(1), 414–434, doi:10.1093/gji/ggt513.

Ryder, I., A. Rietbrock, K. Kelson, R. Bürgmann, M. Floyd, A. Socquet, C. Vigny, and D. Carrizo (2012), Large extensional aftershocks in the continental forearc triggered by the 2010 Maule earthquake, Chile, *Geophys. J. Int.*, *188*, 879–890, doi:10.1111/j.1365-246X.2011.05321.x.

Sato, T., S. Hiratsuka, and J. Mori (2012), Coulomb stress change for the normal-fault aftershocks triggered near the Japan Trench by the 2011 Mw 9.0 Tohoku-Oki earthquake, *Earth Planets Space*, *64*(12), 1239–1243, doi:10.5047/eps.2012.04.003.

Schurr, B., et al. (2014), Gradual unlocking of plate boundary controlled initiation of the 2014 Iquique earthquake, *Nature*, *512*, 299–302, doi:10.1038/nature13681.

Seeber, L., and J. G. Armbruster (2000), Earthquakes as beacons of stress change, *Nature*, *407*, 69–72, doi:10.1038/35024055.

Shinohara, M., et al. (2012), Precise aftershock distribution of the 2011 off the Pacific coast of Tohoku Earthquake revealed by an ocean-bottom seismometer network, *Earth Planets Space*, *64*(12), 1137–1148, doi:10.5047/eps.2012.09.003.

Smith, W. H. F., and D. T. Sandwell (1997), Global sea floor topography from satellite altimetry and ship depth soundings, *Science*, *277*, 1956–1962.

Tassara, A., and A. Echaurren (2012), Anatomy of the Andean subduction zone: Three-dimensional density model upgraded and compared against global-scale mo, *Geophys. J. Int.*, *189*, 161–168, doi:10.1111/j.1365-246X.2012.05397.x.

Tilmann, F., T. J. Craig, I. Grevemeyer, B. Suwargadi, H. Kopp, and E. Flueh (2010), The updip seismic/aseismic transition of the Sumatra megathrust illuminated by aftershocks of the 2004 Aceh-Andaman and 2005 Nias events, *Geophys. J. Int.*, *181*, 1261–1274, doi:10.1111/j.1365-246X.2010.04597.x.

Toksöz, M. N., A. F. Shakal, and A. J. Michael (1979), Space-time migration of earthquakes along the North Anatolian Fault and seismic gaps, *Pure Appl. Geophys.*, *117*, 1258–1270.

von Huene, R., J. Corvalán, E. R. Flueh, K. Hinz, J. Korstgard, C. R. Ranero, W. Weinrebe, and C. Scientists (1997), Tectonic control of the subducting Juan Fernández Ridge on the Andean margin near Valparaiso, Chile, *Tectonics*, *16*(3), 474–488.

Wesnousky, S. G. (2006), Predicting the endpoints of earthquake ruptures, *Nature*, *444*(7117), 358–360, doi:10.1038/nature05275.

Ziv, A., and A. M. Rubin (2000), Static stress transfer and earthquake triggering: No lower threshold in sight?, *J. Geophys. Res.*, *105*, 13,631–13,642.